UiO : Department of Physics
University of Oslo

Using Fault Network Characteristics to Predict Local and Global Damage Accumulation

Gabriel Sigurd Cabrera

Master's Thesis, Spring 2021

Abstract

There are many complex factors that govern the development of fracture networks and the timing of macroscopic failure in rock. So far, we lack a unifying theory to predict fracture development in heterogeneous rock, and the corresponding timing of macroscopic failure. To better understand the factors that most strongly influence fracture development and impending macroscopic failure, we analyze the characteristics of fracture networks in rock under increasing differential stress. These characteristics describe the fracture volume, fracture orientation, fracture length, fracture aperture, and spacing between fractures in a network.

We train extreme gradient boosting (XGBoost) machine-learning models with these features to predict the change in fracture volume in local subvolumes throughout the rock (i.e., local failure) and the stress distance (as a proxy for time) to macroscopic failure (i.e., global failure). We train models on data from eight individual experiments on several rock types: Carrara marble, Westerly granite, and monzonite. The resulting models exhibit a wide range of R^2-values, with scores up to 0.99 for some experiments.

We examine the Shapley Additive Explanation, SHAP, values to determine which fracture network characteristics exert the strongest impact on local and global failure. When the models predict the change in total fracture volume in sub-volume, the volume of individual fractures has the highest feature importance, followed by the fracture orientation, aperture, and fracture. We observe that subvolumes that decrease in fracture volume are correlated to larger fracture lengths and apertures. In most cases, we find that a high volume of individual fractures is also associated with subvolumes that decrease in fracture volume.

When the models predict the stress distance to failure, the fracture orientation is the most important feature, followed by the minimum distance between fractures, the fracture length, the fracture aperture, and the volume of individual fractures. In models where the fracture aperture has a high importance, there is a negative trend in the fracture aperture as failure approaches. Changes in fracture length with approaching failure varied by rock type. The minimum distance between fractures decreases as we approach failure, implying increased localization. We also observe an increase in the volume of individual fractures. As failure approaches, the fractures orient their shortest axis (the eigenvector of their smallest eigenvalue) to a mean angle of 64° from the maximum compression direction, consistent with Mohr-Coulomb theory.

Acknowledgements

A warm thank you to my fantastic advisors: Jessica Ann McBeck, François Renard, and Morten Hjorth-Jensen, for all the much needed guidance!

Contents

CHAPTER 1

Introduction

Understanding the factors that promote and inhibit the growth and interaction of microfractures are a key component in understanding how earthquakes occur. Because crustal faults can heal in the interseismic period, earthquake nucleation requires the breakage of intact rock, and not only sliding on frictional surfaces. Therefore, understanding fracture propagation is a crucial component to earthquake prediction.

Microfractures are discontinuities in rock that form as a result of deformation. Earthquakes can produce distributed microfractures and damage in rocks. The grain structure of rocks, such as sandstone and limestone, can also introduce preexisting weaknesses into rocks that nucleate microfractures.

Laboratory experiments reveal the development of microfractures in rocks under triaxial compression with X-ray microtomography. As the differential stress on a rock sample increases, fractures elongate, growing outwards from their tips. This growth changes orientation over time, first propagating parallel to the maximum compression direction, and then more oblique to it, depending on the applied confining stress [Wu et al., 2000]. Eventually, the volume of the fracture network grows significantly, leading to fracture coalescence into one or more shear bands [Wu et al., 2000, Golshani et al., 2006, Bordignon et al., 2015], regions of significant weakness in the rock that often develop preceding macroscopic failure [Meyers, 2001].

Identifying correlations between the properties of fracture networks and their rate of growth, as well as their time to failure could help us identify earthquake precursors [J. A. McBeck, Aiken et al., 2020]. Because we currently lack an analytical method to predict the coalescence and localization of hundreds and thousands of fractures [Bonamy and Bouchaud, 2011], we develop machine learning models from experimental data. Our goal is to create models that predict the change in the volume of fractures in rock, i.e., local failure, and others that predict the timing of macroscopic failure in core samples under increasing triaxial compression, i.e., global failure.

For the machine learning models, we select features from our data, such as the spacing between individual fractures, and the volume, length, and orientation of individual fractures. Previous work indicates that features are linked to fracture propagation [Dahlen, 1984, Wu et al., 2000, J. McBeck et al., 2019; Kandula et al., 2019]. Using Shapley additive explanations (SHAP), we will identify

which features are the most important in the model prediction and analyze their evolution with the two target values. We shed light on the mechanisms that cause fracture propagation and coalescence, and macroscopic failure by comparing our results with existing fracture mechanics frameworks and prior experiments.

CHAPTER 2

Background

2.1 Fracture Development in Rocks During Triaxial Compression

In rock, fractures may propagate due to increases in loading, and subsequent interaction between neighboring fractures. Macroscopic failure, in which a system can no longer support the applied load, can occur in response to fracture interaction. Under triaxial compression, rock heterogeneity can produce shear and tensile stress concentrations, leading to the growth of preexisting microcracks at tensile stress concentrations, such as at the tips of preexisting weaknesses [Paterson, 1978]. Because the internal stresses within a heterogeneous rock structure are not distributed uniformly, stress concentrations can produce microcracks and flaws in the structure.

As these fractures grow, the stress concentrations at the fracture tips propagate further away from their point of origin, orienting themselves parallel to the maximum compression direction [Paterson, 1978]. Eventually, both stable and unstable growth may lead to coalescence with neighboring fractures [Paterson, 1978]. When multiple fractures coalesce in a rock sample, this strain localization can produce shear zones, then the accumulation of strain within these bands causes macroscopic failure [Wu et al., 2000, Bordignon et al., 2015].

2.2 Characteristics of Fractures that Predict the Growth of Individual Fractures

Previous work has shown that a fracture's orientation, length, and aperture, as well as the characteristics of its network, can be used to predict its growth using machine learning [J. McBeck et al., 2019]. We extract these characteristics using X-ray tomography. X-ray tomography coupled to an X-ray transparent deformation apparatus (HADES) allows us to extract the characteristics of a fracture network under triaxial loading in situ.

In such experiments, we place core samples into the deformation apparatus HADES and obtain X-ray tomograms each time we increase the differential stress [Kandula et al., 2019]. The tomograms are 3D fields that show variations in the local density of the material. Thus, we may distinguish fractures from the surrounding intact rock. We then process the tomograms and the corresponding

fracture networks to extract statistics on the fractures' positions, shapes, sizes, and orientations [J. McBeck et al., 2019]. We extract these statistics for spatial regions within the rock samples, meaning that we divide each sample into subvolumes and then calculate the statistics of the population of fractures within each subvolume.

In the present work, we quantify fracture development using the change in the density of fractures per subvolume. We calculate this value each time the differential stress on the sample increases. We will attempt to predict this value using the following geometric characteristics as features: the fracture length, aperture, orientation, and volume. We also use the distance between fractures. We selected these characteristics using concepts from linear elastic fracture mechanics, or LEFM [Griffith, 1921, Isida, 1971, Dahlen, 1984, Wu et al., 2000, J. McBeck et al., 2019].

In X-ray tomography experiments, closing fractures tend to be longer and narrower than opening fractures [J. McBeck et al., 2019]. If there is a correlation between aperture and fracture tip bluntness, a narrow fracture aperture could encourage propagation due to additional shear stress concentrations at its tips [J. McBeck et al., 2019]. We also expect closing fractures to have a more significant shape anisotropy relative to opening fractures. Finally, a fracture's length is proportional to the stress intensity factor at its tips [Jaeger, 2010]. Because the likelihood of fracture propagation depends on the loading, greater fracture lengths can induce an increase in fracture volume [Jaeger, 2010].

The minimum distance between fracture centroids (a measure of fracture spacing) is closely related to the rate of fracture propagation: a higher density of fractures increases propagation probability [Olson, 2007, J. McBeck et al., 2019]. Additionally, if the volume of the individual fractures is large, this characteristic may produce higher densities of fractures, increasing the likelihood of failure [Lockner, 1995].

2.3 Characteristics of Fracture Networks that Predict the Timing of Catastrophic Failure

Fracture network development determines how and when macroscopic failure occurs in the brittle regime. Therefore, fracture networks' geometric and spatial characteristics may help predict whether macroscopic failure is likely to occur. The time to failure can be quantified using the differential stress acting on the rock relative to the differential stress at macroscopic failure. Previous work has predicted the stress distance to failure using fracture networks' geometric and spatial characteristics [J. A. McBeck, Aiken et al., 2020].

The probability of macroscopic failure is linked to fracture volume and fracture coalescence. As the differential stress on heterogeneous rock increases, its fracture networks often increase in volume, and at faster rates near failure [Cartwright-Taylor et al., 2020]. Additionally, the minimum distance between fractures, which is a measure of fracture clustering, can help identify how close a network is to failure as increased clustering has been observed near failure [Wu et al., 2000, J. A. McBeck, Zhu et al., 2021].

The direction in which a fracture propagates changes with loading under triaxial compression. Initially, the orientation of fractures may attain a variety of angles. However, with increasing differential stress, fractures tend to propagate in a direction parallel to the maximum compression direction [Paterson, 1978], and may form arrays of fractures that trend oblique from this direction [Renard, J. McBeck et al., 2018]. Consequently, as a rock approaches failure, the eigenvectors associated with the largest eigenvalues for each fracture tend to orient themselves between 20° and 30° relative to the maximum compression direction [J. A. McBeck, Aiken et al., 2020]. The orientation of a fracture relative to its maximum compression direction can therefore indicate impending failure.

As the average fracture length increases, so does the probability of fracture coalescence. In general, the shape of a fracture significantly influences the dynamics of its propagation and that of the fractures in its vicinity [Olson and Pollard, 1991, Thomas et al., 2017]. The characteristics related to fracture shape (i.e., their length, aperture, and shape anisotropy) can help indicate whether a rock is near failure [J. A. McBeck, Aiken et al., 2020].

CHAPTER 3

Method

3.1 Experimental Conditions

We deform eight core samples under triaxial compression in an X-ray transparent triaxial deformation apparatus (HADES) at the European Synchrotron and Radiation Facility [J. A. McBeck, Aiken et al., 2020]. These cores consist of three monzonite, two Carrara marble, and three Westerly granite samples. The samples are 1.0 cm tall cylinders with diameters of 0.5 cm. Viton polymer jackets surrounding the cores and oil apply the confining stress [Renard, Cordonnier et al., 2016].

We increase the axial stress incrementally such that the confining stresses range from 5 MPa to 35 MPa [J. A. McBeck, Aiken et al., 2020]; we then obtain an X-ray tomogram of the sample during the resting period between each increase (after the stresses have reached equilibrium). The tomogram reveals the parts of the sample that are primarily solid, primarily air, at a resolution of 6.5 µm per voxel [J. A. McBeck, Aiken et al., 2020].

In total, we capture over sixty tomograms per experiment. We use the software AvizoFire™ to denoise the images, filter out the surrounding apparatus, and stitch together the resulting data [Renard, Cordonnier et al., 2016]. This process provides three-dimensional binary arrays in which zeros represent air and ones represent solid rock. The fractures then need to be identified and tracked throughout their formation and propagation [Kandula et al., 2019]. We see a cross-section of one of the time-steps for two experiments (Granite 4 and Marble 2) in Figure A.1.

Finally, the size, shape, and orientation of what we now consider to be individual fractures are extracted, as well as various statistics on the spacing between fractures [J. McBeck et al., 2019].

3.2 Machine Learning Models

Our machine learning algorithm of choice is the decision tree optimized with extreme gradient boosting (XGBoost). While more straightforward ensemble methods (i.e., gradient boosting) can optimize decision trees, XGBoost consistently outperforms these alternatives – such as in the 2015 KDDCup – and improves upon its training speed due to its scalability and ability to account for data sparsity [Chen and Guestrin, 2016].

We employ a grid-search over the model hyperparameters, including the learning rate, the number of model estimators, the subsample ratio of tree columns, the $L1$-regularization term, and the maximum tree depth. To further gauge model performance, we train the model N times, such that each set of models has its own unique, random selection of the dataset (80% training, 20% testing). From each grid-search, we then select the model with the best R^2-score, resulting in a set of N final R^2-scores from which we draw our conclusions.

To limit computing time, we set the value of N to the minimum possible value. We determine this value by running twenty-four grid-searches from $N = 5$ to $N = 100$ and select the smallest N at the point where the mean R^2-score reaches an equilibrium.

We vary the number of models N to assess whether the R^2-score converges for larger N (Figure A.2, Figure A.3). These models only differ in how we split the training and testing data. We see the standard deviation of the R^2-score decreases for increasing N, but not systematically (Figure A.2, Figure A.3). In the remaining analysis, we use results with $N = 25$ for each experiment. Thus, we develop twenty-five models for each experiment differing only in how we split the training and testing data. The selected experiments: Monzonite 3 and Granite 1, have scores that differ significantly, such that these two plots are an excellent example of this instability.

3.3 Feature Extraction

We develop the models to predict the change in total fracture volume ΔV_{tot} within subvolumes throughout the tomogram from one scan acquisition to the next, and the distance to failure, ∇_{D}, acting on the tomogram for individual experiments. We identify individual fractures as groups of at least three thousand connected points of air – these are represented by the number one (i.e., binary true) in each tomogram's post-processed binary array.

We extract the features following the principles of linear elastic fracture mechanics (LEFM) and other criteria of rock mechanics described in the background section. We divide each tomogram into subvolumes before feature extraction and then calculate the characteristics of the fractures in each subvolume. After we extract the characteristics of each fracture, we report the statistics of the characteristics for the population of fractures within each subvolume, including the minimum, 25^{th} percentile, 50^{th} percentile, 75^{th} percentile, and maximum. Our features include the density of fractures per volume, the relative positions of fractures, and the orientation of these fractures relative to the maximum compression direction σ_1. We also account for the geometric properties of the fractures, such as their lengths, L_{max}, apertures, L_{min}, and shape anisotropies, A,

$$A = \frac{1 - L_{\text{min}}}{L_{\text{max}}}, \tag{3.1}$$

[J. A. McBeck, Aiken et al., 2020]. To help compare the importance of the features, one of the features is a random number [J. A. McBeck, Aiken et al.,

2020]. We split the data into training and testing datasets and keep 80% in the training data set.

Table A.1 contains an overview of the features used in each model and their respective abbreviations, which are present in multiple figures and throughout this text.

3.4 Evaluation of Models

We evaluate model performance and feature importance using standard machine learning metrics. We use the coefficient of determination (R^2) and the SHapley Additive exPlanations (SHAP) of our model features.

The R^2-score for a set of N observed points $y_i \in \mathbf{y}$ and N corresponding predicted points $f_i \in \mathbf{f}$ as

$$R^2 = 1 - \frac{\sum_i (y_i - \overline{y})^2}{\sum_i (y_i - f_i)^2}, \tag{3.2}$$

where $\overline{y}$ is defined as the mean value in $\mathbf{y}$.

Lundberg and Lee, 2017 describe how to calculate the SHAP value from machine learning models. We use the `python-pip` package `shap` to calculate the SHAP programmatically. In each experiment, we develop several models, leaving us with several sets of feature importance (one per model), so we define the cumulative importance I for a single feature across N models using the method described in J. A. McBeck, Aiken et al., 2020,

$$I = \sum_i^N R^2 \cdot \frac{s_f}{s_{\max}}, \tag{3.3}$$

such that s_f is the mean of the absolute values of the SHAP for the given feature, and $s_{\max}$ is the maximum mean absolute SHAP over all features.

Additionally, we wish to determine how feature importance varies across experiments. Therefore, we must normalize the cumulative importance before comparing models from different experiments, given that N may vary across them. We accomplish this step by dividing each importance over the number of models in question, yielding the normalized cumulative importance.

$$I_{\text{norm}} = \frac{1}{N} \sum_i^N R^2 \cdot \frac{s_f}{s_{\max}}. \tag{3.4}$$

CHAPTER 4

Results

4.1 The Phases of Rock Deformation by Rock Type

We observe the differential stress applied to each experiment as functions of their respective axial strains in Figure A.4. The trends in each sub-figure correspond to the three main stages of rock deformation under triaxial compression.

1. Initially, we have a linear period of stress vs. strain, in which elastic deformation occurs, and the material can return to its initial configuration assuming a subsequent decrease in pressure (reversible strain).

2. Once the linear portion ends and the slope changes, the material begins to experience ductile deformation – after this point, there is irreversible damage to the material (irreversible strain).

3. After applying even more pressure that we reach macroscopic (or catastrophic) failure; this is not visualized in Figure A.4 since measurements ceased as soon as we reached failure under experimentation.

Each of the experiments in Figure A.4 has a unique trend, with similarities across rock types. Marble 1 and Marble 2 appear to evolve similarly to one another, with relatively smooth transitions from elastic to inelastic deformation. Additionally, their inelastic portions take place over a wide range of axial strains.

Monzonite 3 and Monzonite 4 also resemble each other, with long-lasting elastic deformation followed by a short inelastic deformation before failure. Monzonite 5, on the other hand, behaves quite uniquely, with an evident transition between the elastic and inelastic parts of its deformation and a long inelastic deformation across an extensive range of axial strains.

Granite 1, Granite 2, and Granite 4 follow trends, not unlike Monzonite 3 and Monzonite 4, but tend to have much smoother elastic-inelastic transitions with respect to the other rock types. The three granite experiments also have some of the shortest inelastic portions of deformation and quickly begin to fracture after this point is reached.

4.2 Predicting the Change in Fracture Volume

Model Success

We assess how well each experiment's models perform with respect to one another when considering their R^2-scores for the target ΔV_{tot} (Figure A.5).

Figure A.5 shows how the models perform when they predict ΔV_{tot} in each experiment. The models developed with the granite experiments produce the best prediction of ΔV_{tot}, while the marble and monzonite produce lower R^2-scores on average. The model developed with Monzonite 5 produced several acceptable models comparable to those based on granite, but these are outliers as most monzonite models have lower R^2-scores.

Figure A.6 shows a wide range in R^2-scores when we change how we split the training and testing data. To assess why these differences occur, we show the training and testing data sets for the two best performing and two worst-performing models developed with the Monzonite 3 data. Figure A.6 shows that the predictive ability of the poorly performing models (for experiment Monzonite 3) arises from the heterogeneous nature of rock deformation. In particular, the training data tends to perform reasonably well, even when the testing set performs poorly (e.g., Figure A.6d).

Identifying the Characteristics that Control Fracture Development

We analyze the importance of the features in our best-performing models trained to predict ΔV_{tot}. We quantify feature importance using the Shapley Additive Explanation values, SHAP. The SHAP measure estimates how vital a given feature is in predicting the model target (see Section 3.4). We examine the SHAP metric of models with R^2-score above 0.7.

Although the R^2-scores for the granite models consistently perform well, the most critical features differ between Granite 1, Granite 2, and Granite 4 (Figure A.7). In Figure A.7, The best-performing models (Granite 1) differ from the other granite models in that the individual fracture volume (v) is not a factor in their success, while v is among the important features for Granite 2 and Granite 4.

The features that are most important in the experiment Granite 1 include the minimum distance between fracture centroids (d_{min}), followed by the fracture aperture (L_{min}). The other features do not appear to affect the models' performances, except for the fracture length (L_{max}).

The models based on Granite 2 and Granite 4 depend on the individual fracture volume (v). Granite 2 also depends on the fracture length (L_{max}). The second most important feature for the models created using the Granite 4 experiment is the shape anisotropy (A).

We now examine the distribution of SHAP values for the marble experiments and disregard any models that fail to reach the R^2-score threshold of 0.7. We, therefore, only examine the influence of features in the Marble 2 models.

Figure A.8 shows that the individual fracture volume (v) is the most significant contributor to model performance for experiment Marble 2, followed by the distance between fracture centroids (d_c) and the fracture length (L_{max}).

Monzonite is the rock type that yielded the lowest R^2-scores of the examined rock types. Thus, only one model produced R^2-scores above 0.7.

Figure A.9 shows that the most crucial feature for Monzonite 5 is the orientation of the smallest fracture dimension relative to the maximum compression direction (θ_1), followed by the fracture aperture (L_{min}), the individual fracture volume (v), and the fracture length (L_{max}).

Figure A.10 shows the most important features of each rock type, and not by experiment, as in the previous three figures. The features that contribute the most to each rock type vary, though all the rock types depend on the individual fracture volume (v). Note, the marble and monzonite curves represent the Marble 2 and Monzonite 5 experiments, respectively, because the other marble and monzonite experiments did not yield R^2-scores above 0.7.

The most critical features overall in the granite models are the individual fracture volume (v) and the minimum distance between fracture centroids (d_{min}), followed by the fracture length (L_{max}) and the fracture aperture (L_{min}).

Overall, the individual fracture volume (v) has the most effect on model performance across all rock types, followed by the fracture length (L_{max}) and fracture aperture (L_{min}). Otherwise, the other features' importances vary across rock types – in the case of the marble models, the distance between centroids (d_c) significantly influences the model score, but not in the other rock types.

In the granite models, the minimum distance between fracture centroids (d_{min}) is highly influential. In contrast, the monzonite models and the granite models, to a lesser extent, are heavily affected by the orientation of the smallest fracture dimension concerning the maximum compression direction (θ_1).

Evolution of the Characteristics that Control Fracture Development

We now examine the evolution of the most important features according to the SHAP values with respect to the change in total volume ΔV_{tot}.

Figure A.11 shows how the fracture aperture changes with the change in total volume ΔV_{tot}. The experiments selected – Granite 1, Granite 2, and Monzonite 5 – are when the fracture aperture has the highest normalized cumulative importance. Using a polynomial fitting technique, the line of best fit illustrates that there are larger apertures in these experiments when fractures are predominantly closing, producing negative ΔV_{tot}, and smaller apertures when fractures are predominantly opening, producing positive ΔV_{tot}.

Figure A.12 shows that the fracture length evolves with the change in total volume, ΔV_{tot}. The experiments selected – Granite 1, Granite 2, and Monzonite 5 – are those in which the fracture length has the highest normalized cumulative importance. The line of best fit illustrates that in these experiments, there are more extended fractures when fractures are predominantly closing and shorter fractures when fractures are predominantly opening.

Figure A.13 shows the volume of individual fractures relative the change in total volume ΔV_{tot}. The experiments selected – Marble 2, Granite 4, and Monzonite 5 – are those in which the volume of individual fractures has the highest normalized cumulative importance. The line of best fit illustrates that we cannot universally tie v to the proportion of opening and closing fractures (Figure A.13a). In Figures A.13b and A.13c, there is a trend in which a higher proportion of closing fractures indicates a higher v, while a higher proportion of opening fractures is linked to lower v.

In Figure A.14, we show the minimum distance between fractures relative to the change in total volume ΔV_{tot}. Granite 1 is the only experiments in which its models had a high normalized cumulative importance in d_{min}. The line of best fit illustrates that in this experiment, d_{min} increases as a function of the change in total volume, with a major increase in d_{min} for subvolumes where the volume of fractures is increasing.

Overall, the feature values as functions of the change in total volume seem to follow distinct and apparent trends, especially when the feature in question is of high importance. We see that there exists a clear relationship between the scale of the change in volume between multiple features, a relationship that indicates microfracture characteristics depend on whether there are more opening or closing fractures.

4.3 Predicting the Proximity to Failure

Model Success

We now assess how well each experiment's models perform with respect to one another with respect to their R^2-scores for the target ∇_{D}. Figure A.15 shows the model performance in predicting the distance to failure, ∇_{D}.

The granite and marble models perform similarly well, while the R^2-values for monzonite are generally worse (Figure A.15). Experiment Monzonite 4 performed particularly poorly, while Monzonite 3 and Monzonite 5 resembled Marble 1 and Granite 2. Marble 2 and Granite 1 are the top-scoring experiments when the models predict ∇_{D}.

Identifying the Characteristics that Control Distance to Failure

We now analyze the importance of the features in our best-performing models developed to predict ∇_{D} . We quantify feature importance via the SHAP value. The SHAP measure estimates how vital a given feature is in predicting a target (see Section 3.4). We examine the SHAP metric in models with R^2-score above 0.7.

The granite models performed well for all three experiments, so we examine the feature importance for all three of these models (Granite 1, Granite 2, and Granite 4). The most important features are the length (L_{max}), the orientation of the smallest fracture dimension relative to the maximum compression direction (θ_1), and the fracture volume (v) (Figure A.16).

We now examine the SHAP values of the marble models with R^2-scores greater than 0.7 (Figure A.17). The most significant features are the orientation of the

smallest fracture dimension relative to the maximum compression direction, the distance between centroids (d_c), and the fracture aperture (L_{min}).

Figure A.18 summarizes the SHAP for models trained on the monzonite experiments predicting the distance to failure. The monzonite experiments produced the worst model predictions overall, and only Monzonite 3 yielded models with R^2-scores above 0.7.

The most important feature for Monzonite 3 is the orientation of the smallest fracture dimension relative to the maximum compression direction (θ_1), followed by the minimum distance between centroids (d_{min}).

In Figure A.19, the features that contribute the most to each rock type (rather than experiment) vary, except for the orientation of the smallest fracture dimension relative to the maximum compression direction (θ_1), which is the most critical feature across all rock types.

Other than θ_1, The marble models favor the fracture aperture (L_{min}), the distance between centroids (d_c), and the total volume (v_{tot}). In the case of the granite models, the other most important features are the volume of individual fractures (v), the fracture length (L_{max}), and the fracture aperture (L_{min}).

The monzonite models' second, third, and fourth most important features are the minimum distance between fracture centroids (d_{min}), the orientation of the largest fracture dimension relative to the maximum compression direction (θ_3), and the fracture length (L_{max}).

Evolution of the Characteristics that Control Fracture Development

Figure A.20 shows the minimum distance between fractures with the normalized time to failure ∇_D. The experiments selected – Granite 2, Monzonite 3, and Marble 2 – are those in which the minimum distance between fractures has the highest normalized cumulative importance. In these experiments, the minimum distance between fracture centroids tends to decrease as failure approaches.

Figure A.21 shows the fracture aperture relative to the normalized time to failure ∇_D. The experiments selected – Granite 2, Marble 1, and Marble 2 – are those in which the fracture aperture has the highest normalized cumulative importance. The fracture aperture tends to become smaller as failure approaches, but not always by a large margin. This trend may occur as more and more fractures develop, the fracture population includes many smaller fractures, rather than only the preexisting pore space. Under low differential stress, the preexisting pores produce the measurements of the fracture aperture.

Figure A.22 shows the fracture length evolving with respect to the normalized time to failure ∇_D. The experiments selected – Granite 2, Granite 4, and Marble 1 – are those in which the fracture length has the highest normalized cumulative importance. The fracture length has a trend that differs in each experiment. We observe a sudden increase in fracture length near failure for Granite 2 and a more gradual increase near failure for Granite 4. In Marble 1, we observe a continuous decrease in fracture length as failure approaches.

In Figure A.23, we show the orientation of the smallest fracture dimension relative to the maximum compression direction evolving with respect to the normalized time to failure ∇_{D}. The experiments selected – Granite 1, Marble 1, and Monzonite 3 – are those in which some percentile of θ_1 has the highest normalized cumulative importance. In these experiments, θ_1 varies in trend, but always ends up between 60 and 70° from σ_1. More specifically, Granite 1 takes a stable orientation until failure approaches, then increases quickly to 77°. Marble 1 decreases from an average angle of 76° and reaches an average of 65°. Monzonite decreases in visible steps from 90° to an average of 60°.

CHAPTER 5

Discussion

5.1 Characteristics that Control the Change in Fracture Volume

Many of the experiments produced models that predict the change in fracture volume with high accuracy: the granite models all resulted in R^2-scores above 0.80, with Granite 1's average R^2-score close to 0.99. Monzonite 5 and Marble 2 also managed to yield a few models with scores above 0.80. In summary, we successfully trained machine learning models to predict the change in total volume for granite, and some of the other experiments.

Generally, the experiments whose features have more clustered distributions result in better model performance, while features with irregular values produce worse models. The model performance is governed by a unique subset of features that varies by experiment.

Only the granite and monzonite models depend strongly on the fracture aperture. In the models where they have high importance, the 25^{th} and 50^{th} percentile of L_{min} depend on the change in total volume. If most fractures are closing (a negative change in total volume), the fracture aperture tends to be larger than when there are more opening fractures, consistent with prior observations [J. McBeck et al., 2019]. In addition, we observe larger negative changes in total volume with larger apertures (Figure A.11).

In the models where the fracture length, L_{max}, has high importance (Granite 2 and Monzonite 5), we observe the same trends as the fracture aperture (Figure A.12). The larger the fracture length, the more likely most of the fractures are closing, producing a negative change in total volume. While the trends in fracture length agree with prior research [Jaeger, 2010, J. McBeck et al., 2019], the trend in fracture aperture does not. Interestingly, the models in which the fracture length is important are the same models in which the fracture aperture is important.

The volume of individual fractures is of high importance in every model except for Granite 1. The fracture volume often correlates with the change in total volume, but not always (Figure A.13). In most of the experiments, we observe higher negative changes in fracture volume associated with higher 50^{th} percentile of v. Additionally, the 50^{th} percentile of v is more important in models when it increases as the experiment approaches failure. This evolution may be

indicative of acceleration in the growth of the fracture network as it approaches failure. Thus, experiments that experience systematic increasing fracture volume produce models that exploit this reliable feature.

The minimum distance between fracture centroids did not exhibit high importance in most models, except for those trained on Granite 1. In this experiment, fracture closing produces a small minimum distance between fractures. For slightly larger minimum distances, we see a mixture of increases and decreases in the total fracture volume. Larger amounts of opening fractures produce larger minimum distances between fractures (Figure A.14). In the other experiments, no such trends are identifiable. Prior work has shown that a high degree of fracture clustering increases the likelihood of propagation [J. McBeck et al., 2019].

5.2 Characteristics that Control the Distance to Failure

For the models that predict the time to failure, three experiments yielded models who's mean R^2-scores equal or surpassed 0.80: Granite 1, Marble 2, and Granite 4. When training a machine learning model on the change in total volume, all three experiments yield models with scores greater than or equal to 0.80, indicating that there is some overlap in the characteristics that control the distance to failure and those that control the change in total volume. Some models trained on Marble 1, Monzonite 3, and Granite 2 also had good scores (R^2-score above 0.75).

The minimum distance between fractures has high importance in the models trained on Granite 2, Monzonite 3, and Marble 2 (Figure A.20). The minimum and 75^{th} percentiles of $d_{\min}$ decrease in value over time, highlighting the increasing fracture density as the fracture network approaches failure, similar to previous work [Tapponnier and Brace, 1976, Wu et al., 2000, Golshani et al., 2006, Cartwright-Taylor et al., 2020]. Similarly, the volume of individual fractures has high importance in experiments Granite 1, Granite 2, and Marble 2. In these experiments, the evolution of v demonstrates that fractures grow as the network approaches failure, consistent with previous work [Golshani et al., 2006, Tapponnier and Brace, 1976, J. A. McBeck, Zhu et al., 2021].

Next, the fracture aperture $L_{\min}$ decreases as failure approaches for every experiment (Figure A.21), though its importance is limited to experiments Granite 2, Granite 4, Marble 1, and Marble 2. These observations indicate that the fracture aperture can help predict the time to failure, but not in all cases: this result did not apply to the monzonite experiments, where the fracture aperture was of little importance.

The fracture length also evolves throughout all of the experiment, though this evolution is not consistent across rock types (Figure A.22). In the marble experiments, the mean and variance of the minimum and 25^{th} percentiles of $L_{\max}$ decrease as we approach failure. In the monzonite experiments, these values decrease in mean and an increase in variance. In Granite 2 and Granite 4, their means increase near failure, which is consistent with prior observations in granite [Golshani et al., 2006]. Note that the fracture length has a medium

to high importance in the models trained on Granite 1, Granite 2, Granite 4, Marble 1, and Monzonite 3.

A decrease in variance of fault length implies that the lengths are becoming more uniform. Thus, we observe an increase in fracture length homogeneity in the marble experiments, and an increase in the variety of fracture lengths in the other experiments. Marble may experience more homogeneous fault network development that the other rock types because marble is composed of cemented grains that can influence fracture growth. The grain structure can limit the extent of fractures, producing fracture networks with a more uniform distribution of fracture lengths than the granite and monzonite rocks [J. A. McBeck, Aiken et al., 2020].

While the orientation of the largest fracture dimension relative to the maximum compression direction did not have very high importance in any of the experiments, the orientation of the smallest fracture dimension was critical to most of the models; specifically, those trained on Monzonite 3, Marble 1, Granite 1, Granite 2, and Granite 4. In these models, the 75^{th} percentile of θ_1 had a final average of $64.4°$ to σ_1, with minimal variance (Figure A.23). These values always increase near failure in the granite experiments but decrease near failure in the others. Previous work indicates that the orientation of the largest fracture dimension relative to the maximum compression direction first trends towards zero degrees, then towards thirty degrees as failure approaches [Tapponnier and Brace, 1976, J. McBeck et al., 2019]. Instead, we observe a consistent trend for the orientation of the smallest fracture dimension.

CHAPTER 6

Conclusion

We developed machine learning models to predict the change in the total volume of fractures (local failure) and distance to macroscopic failure (global failure) with an acceptable success rate. Many models yielded R^2-scores above 0.80, with some near 0.99. The model performance varied by experiment. Each model had a slightly different set of highly important features, although some features were universally important.

For the change in the total volume of fractures, the importance of the volume of individual fractures was significant across almost all of the experiments. This importance was possibly due to the correlation between decreases in the fracture volume and higher volumes of individual fractures in many experiments. The fracture length was also important universally, possibly due to the observed correlation between decreases in the fracture volume and higher lengths.

For the distance to failure, the fracture orientation was the most important feature across experiments. The orientation of the fractures' smallest axes tend to move towards an average angle of 64° from the maximum compression direction. While there were no other universally important features, the fracture aperture, and fracture length contributed significantly to model performance, although there were varying trends in their values across different experiments.

Appendices

APPENDIX A

Tables and Figures

A.1 Tables

Table A.1: An overview of each feature's symbolic representation or abbreviation (e.g., McBeck et al., 2020).

Feature	**Symbol**	**Unit**
The minimum distance between fracture centroids	$d_{\min}$	voxels
The orientation of the minimum fracture dimension relative to the maximum compression direction	θ_1	degrees
The orientation of the maximum fracture dimension relative to the maximum compression direction	θ_3	degrees
The fracture aperture (i.e., width)	$L_{\min}$	voxels
The fracture length	$L_{\max}$	voxels
The fracture shape anisotropy	A	none
The volume of individual fractures	v	voxels
The distance between fracture centroids	d_{c}	voxels
The total fracture volume	v_{tot}	voxels
A random number	$rand$	none

A.2 Figures

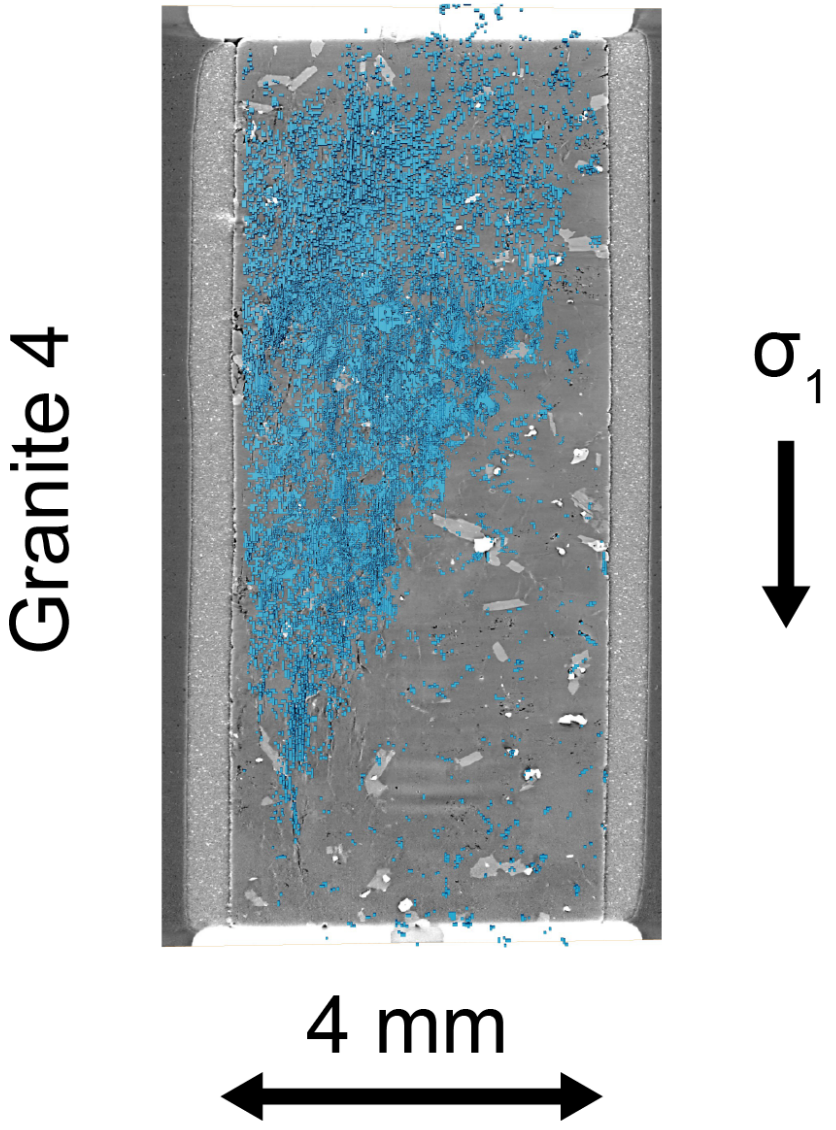

Figure A.1: Slices from the tomograms for experiment Granite 4 while under triaxial compression, prior to failure. The fracture network is highlighted in blue.

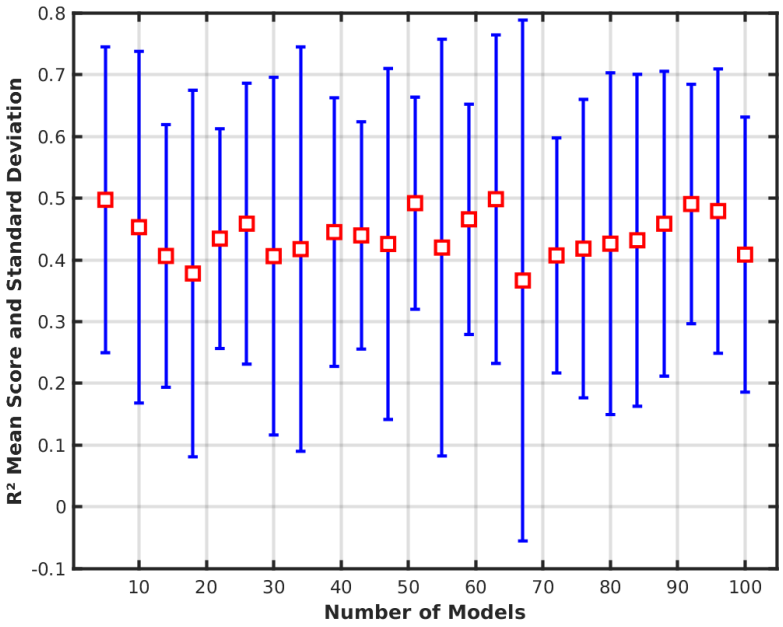

Figure A.2: The mean and standard deviation of the R^2-scores for multiple sets of models using the experiment Monzonite 3 where the number of models in each set is shown on the x-axis. The x-axis represents the number of models over which the mean and standard deviation are being taken. At $x = 10$ for example, the mean was calculated for ten unique models. Every single model used in this figure has a unique training dataset, selected by random split prior to training.

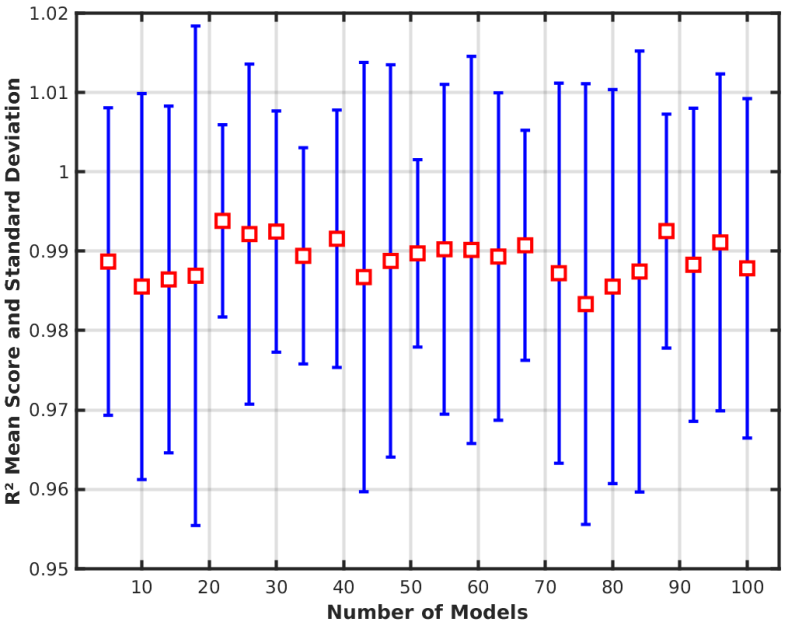

Figure A.3: The mean and standard deviation of the R^2-scores for multiple sets of models created using the experiment Granite 1, where the number of models in each set is shown on the x-axis. The x-axis represents the number of models over which the mean and standard deviation are being taken. At $x = 10$ for example, the mean was calculated for ten unique models. Every single model used in this figure has a unique training dataset, selected by random split prior to training.

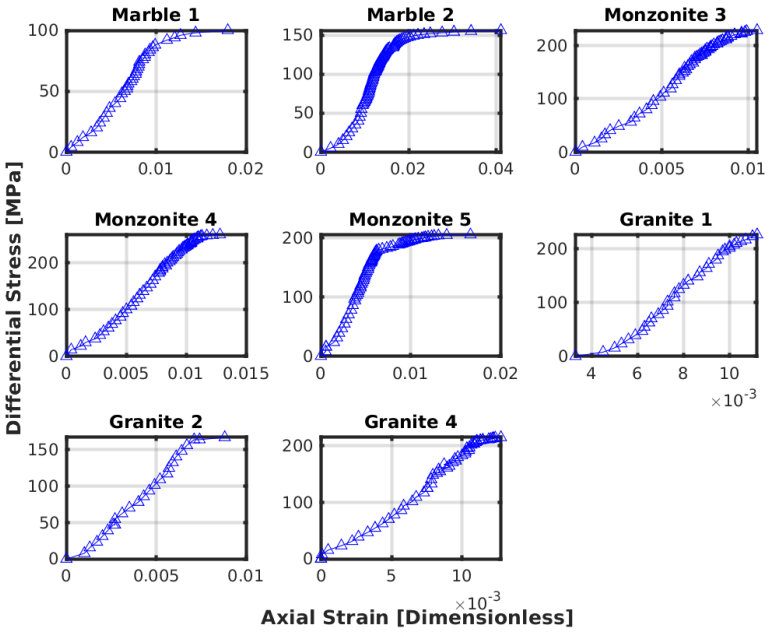

Figure A.4: The differential stress in each rock experiment shown relative to its respective axial strain, as they were compressed in the HADES apparatus. The experiment label is shown above each subplot, and the axis labels apply to all subplots.

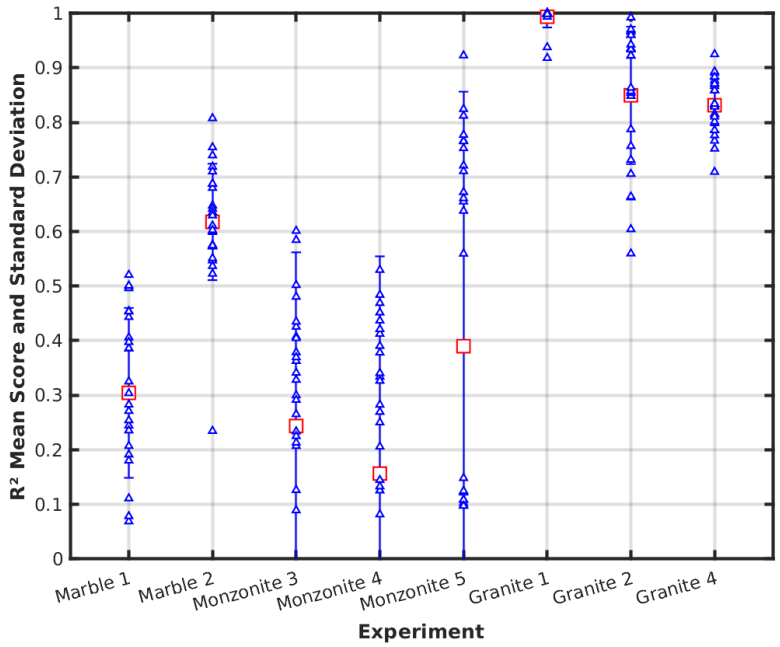

Figure A.5: R^2-scores of each rock type and the average $\pm$ one standard deviation of the twenty-five models for the target ΔV_{tot}. Each model is created using a unique random split of the full dataset. The red squares represent the mean value of the R^2-scores for an experiment, while the attached blue bars represent their standard deviation. The blue triangles represent the R^2-values themselves.

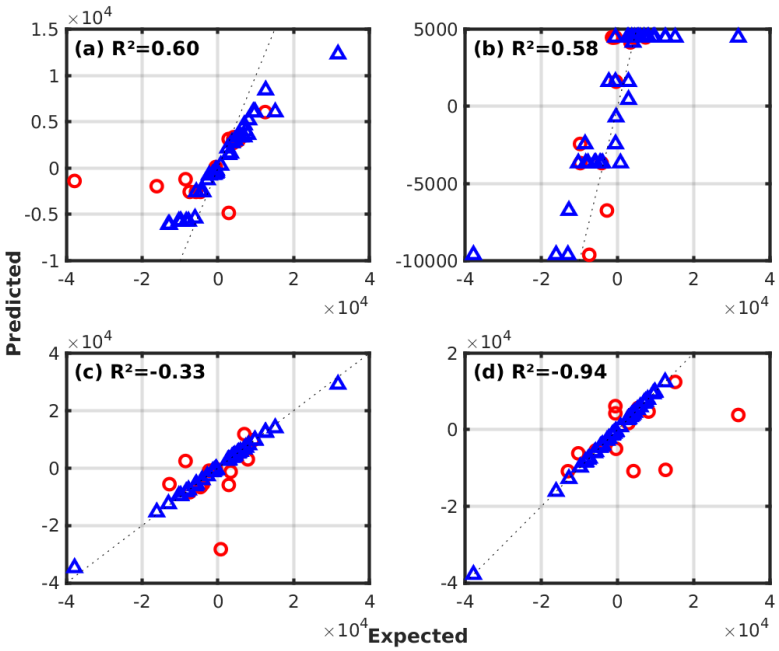

Figure A.6: The expected vs. predicted values for four unique models trained on experiment Monzonite 3 for target ΔV_{tot}, and the models' test-set R^2-scores. Models (a) and (b) represent the two best performing models, while (c) and (d) represent the two worst performing models. The blue triangles represent the training data, while the red circles represent the testing data.

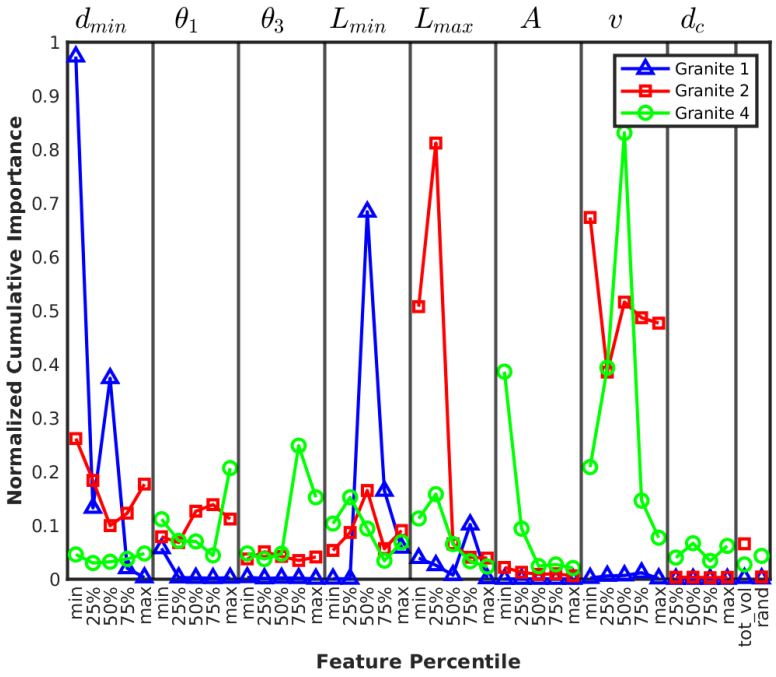

Figure A.7: Normalized cumulative importance of features for models of each granite experiment with R^2-scores above 0.7. The features are split by category via vertical bars, and the statistics of each feature are shown on the x-axis. The symbols and abbreviations above each column are defined in Table A.1.

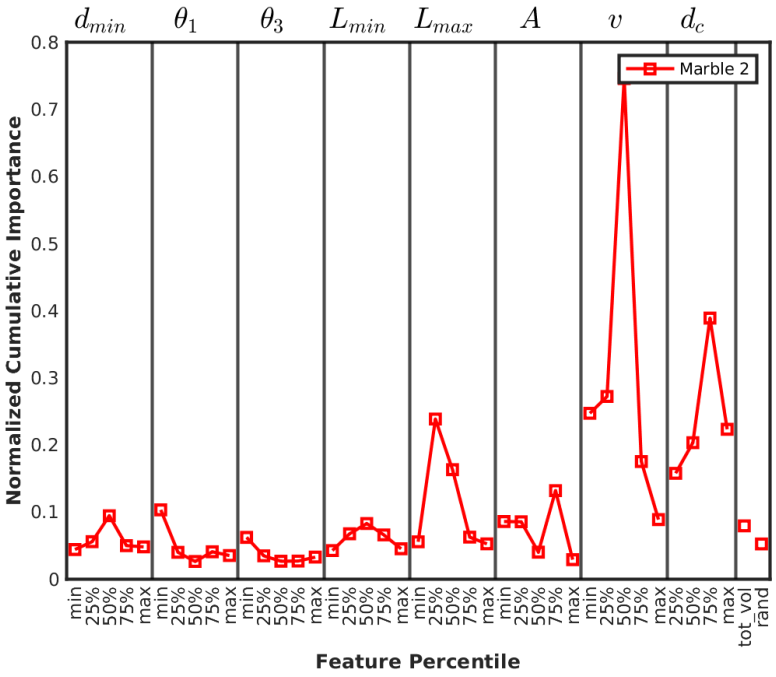

Figure A.8: Normalized cumulative importance of features for models of each marble experiment with R^2-scores above 0.7. The features are split by category via vertical bars, and the statistics of each feature are shown on the x-axis. The symbols and abbreviations above each column are defined in Table A.1.

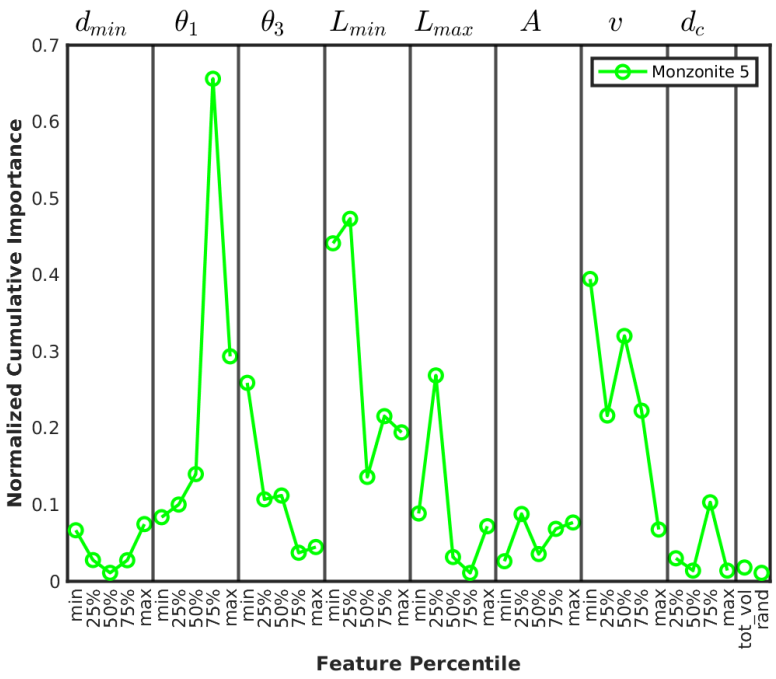

Figure A.9: Normalized cumulative importance of features for models of each monzonite experiment with R^2-scores above 0.7. The features are split by category via vertical bars, and the statistics of each feature are shown on the x-axis. The symbols and abbreviations above each column are defined in Table A.1.

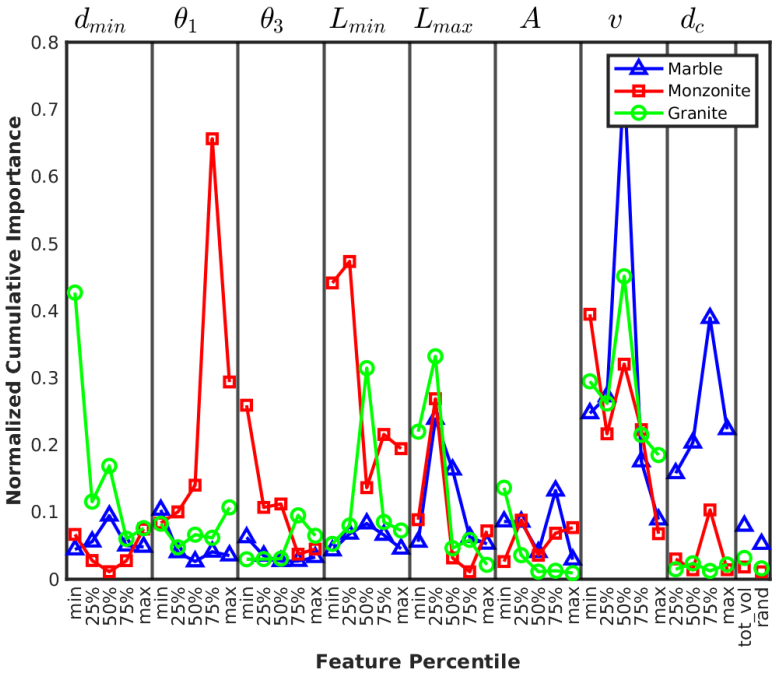

Figure A.10: Normalized cumulative importance of features for models of each rock type with R^2-scores above 0.7. The features are split by category via vertical bars, and the statistics of each feature are shown on the x-axis. The symbols and abbreviations above each column are defined in Table A.1.

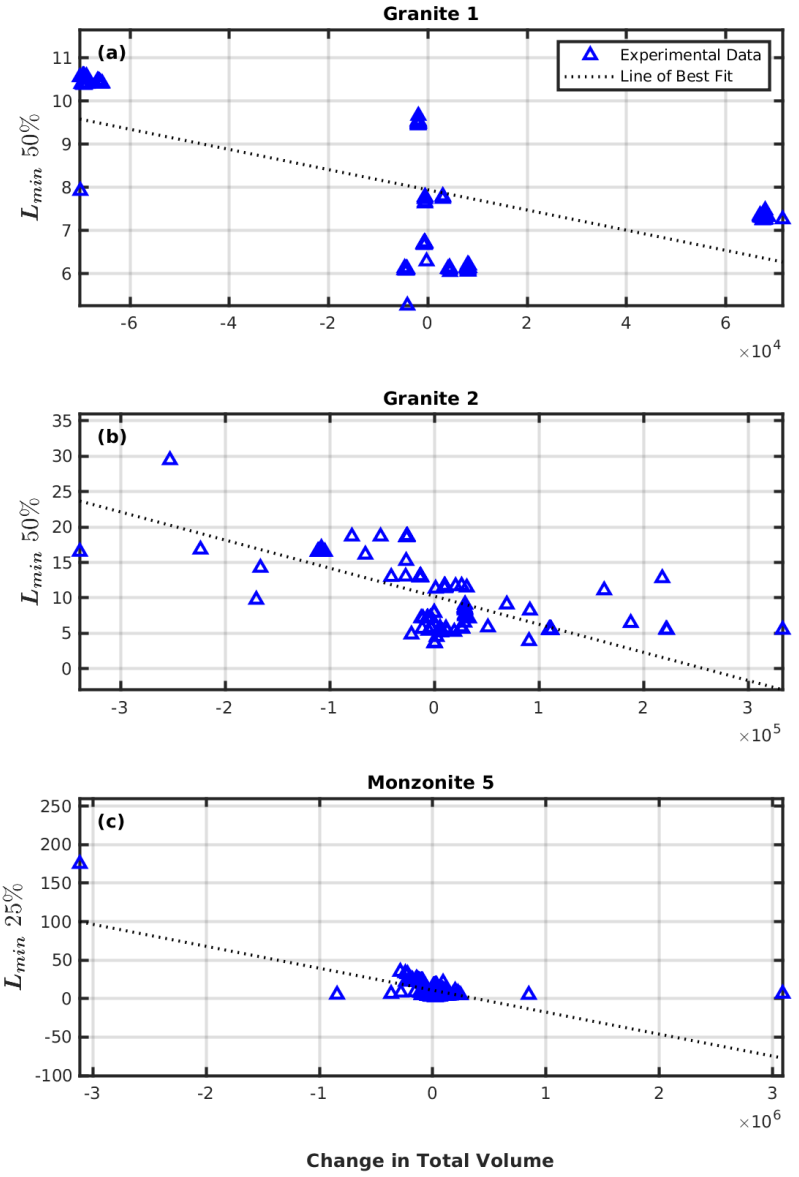

Figure A.11: The percentiles of the fracture aperture $L_{\min}$ with the highest importance for experiments: Granite 1 (a), Granite 2 (b), and Monzonite 5 (c), as functions of the change in total volume ΔV_{tot}. It was in the models for these three experiments that $L_{\min}$ exhibited the highest importance.

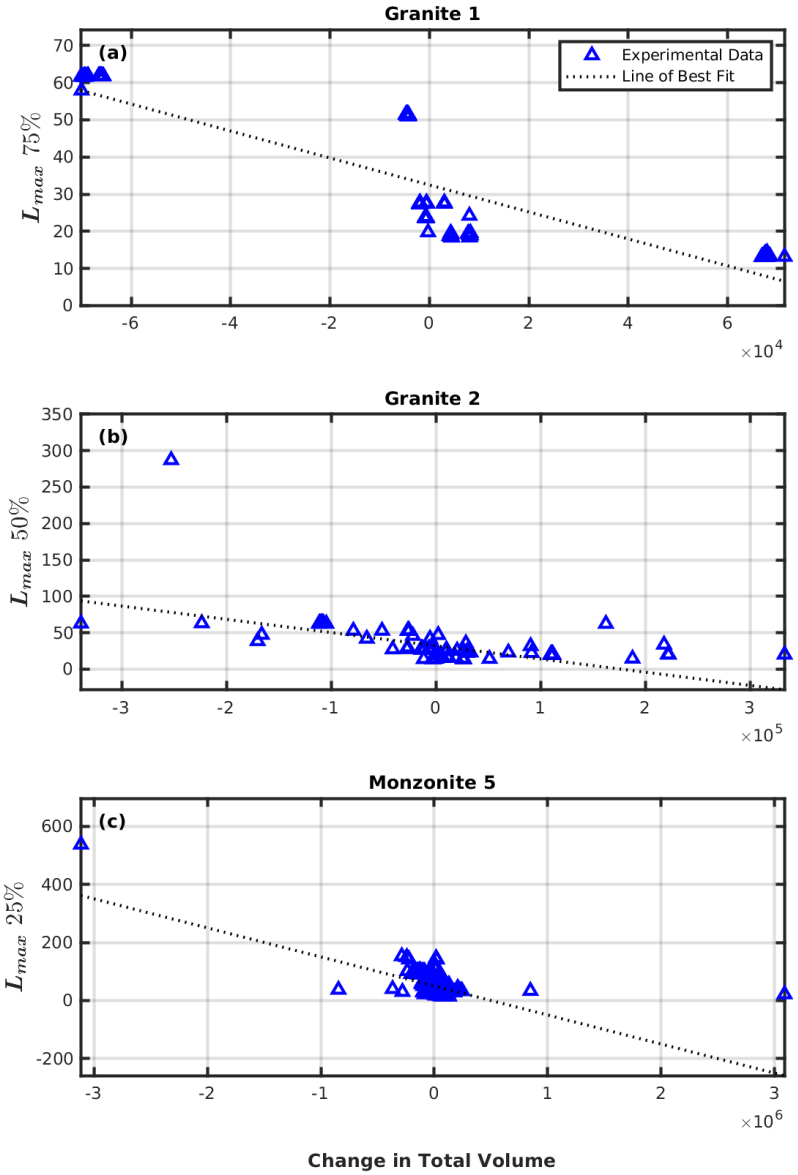

Figure A.12: The percentiles of the fracture length $L_{\max}$ with the highest importance for experiments: Granite 1 (a), Granite 2 (b), and Monzonite 5 (c), as functions of the change in total volume ΔV_{tot}. It was in the models for these three experiments that $L_{\max}$ exhibited the highest importance.

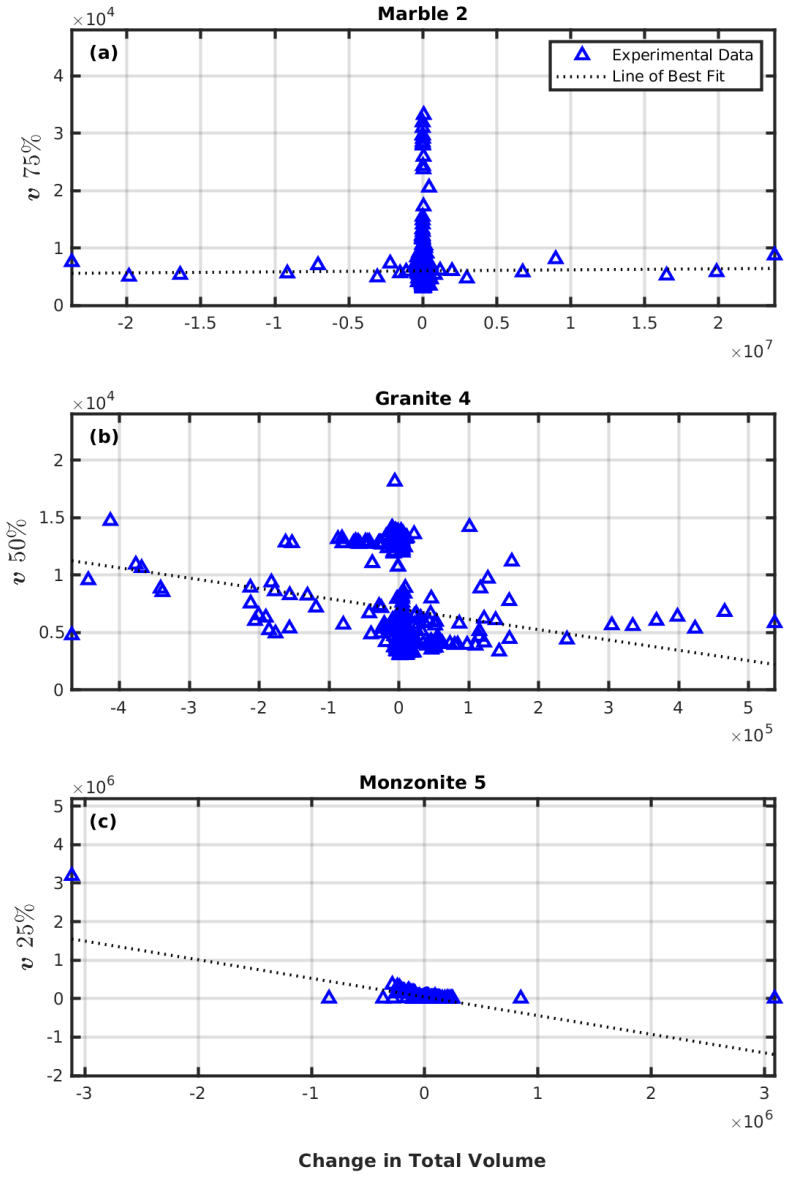

Figure A.13: The percentiles of the volume of individual fracture v with the highest importance for experiments: Marble 2 (a), Granite 4 (b), and Monzonite 5 (c), as functions of the change in total volume ΔV_{tot}. It was in the models for these three experiments that v exhibited the highest importance.

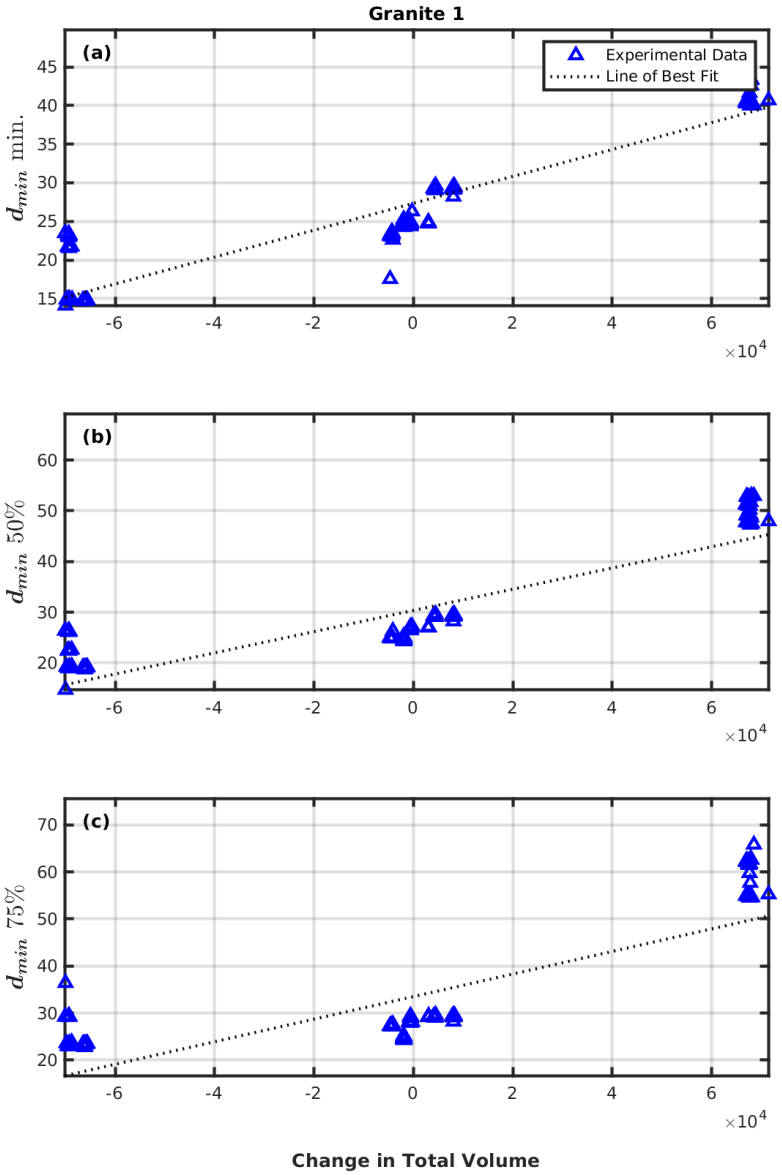

Figure A.14: The minimum, 50$^{\text{th}}$, and 75$^{\text{th}}$ percentile of the minimum distance between fractures d_{min} for experiment Granite 1, as functions of the normalized time to failure ΔV_{tot}. It was only in the models for experiment Granite 1 that percentiles of d_{min} exhibited a high importance.

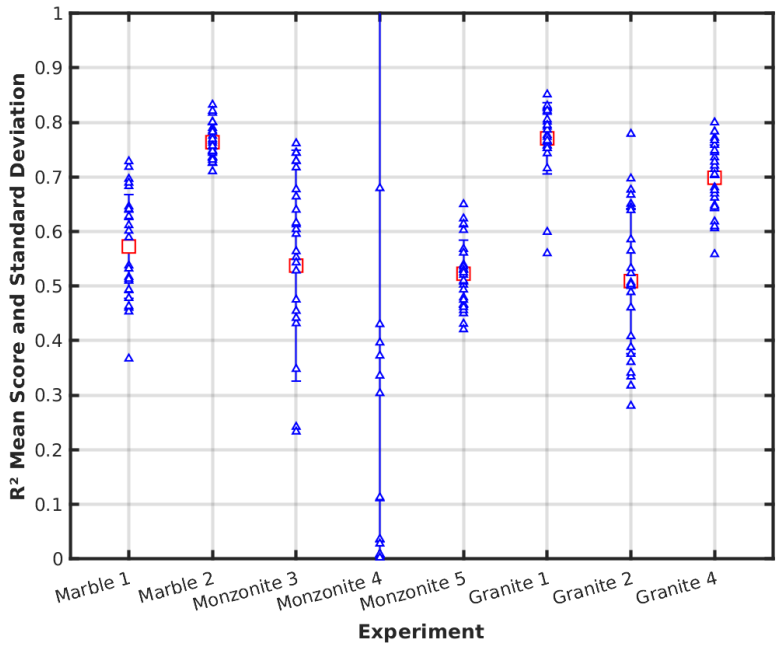

Figure A.15: A comparison of the R^2-scores of each rock type, each averaged over the twenty-five best performing models for the target ∇_D. Each model is created using a unique random split of the full dataset. The red squares represent the mean value of the R^2-scores for an experiment, while the attached blue bars represent their standard deviation. The blue triangles represent the R^2-values themselves. The mean value of the R^2-scores for Monzonite 4 is located below zero.

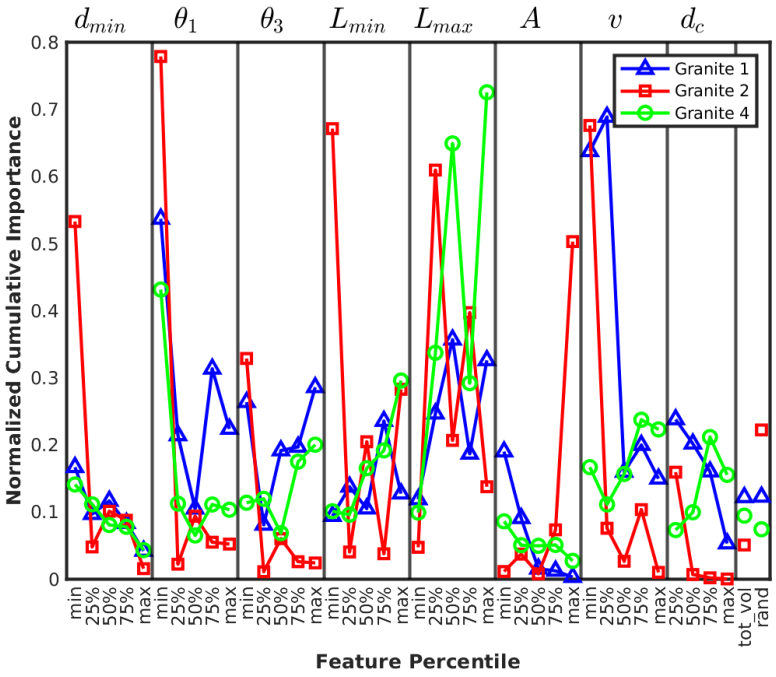

Figure A.16: Normalized cumulative importance of features for models of each granite experiment with R^2-scores above 0.7. The features are split by category via vertical bars, and the statistics of each feature are shown on the x-axis. The symbols and abbreviations above each column are defined in Table A.1.

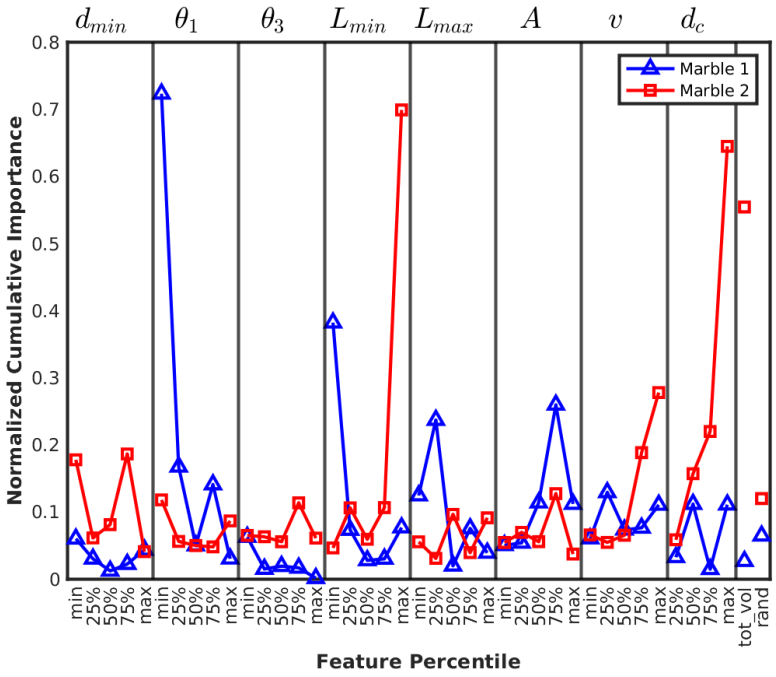

Figure A.17: Normalized cumulative importance of features for models of each marble experiment with R^2-scores above 0.7. The features are split by category via vertical bars, and the statistics of each feature are shown on the x-axis. The symbols and abbreviations above each column are defined in Table A.1.

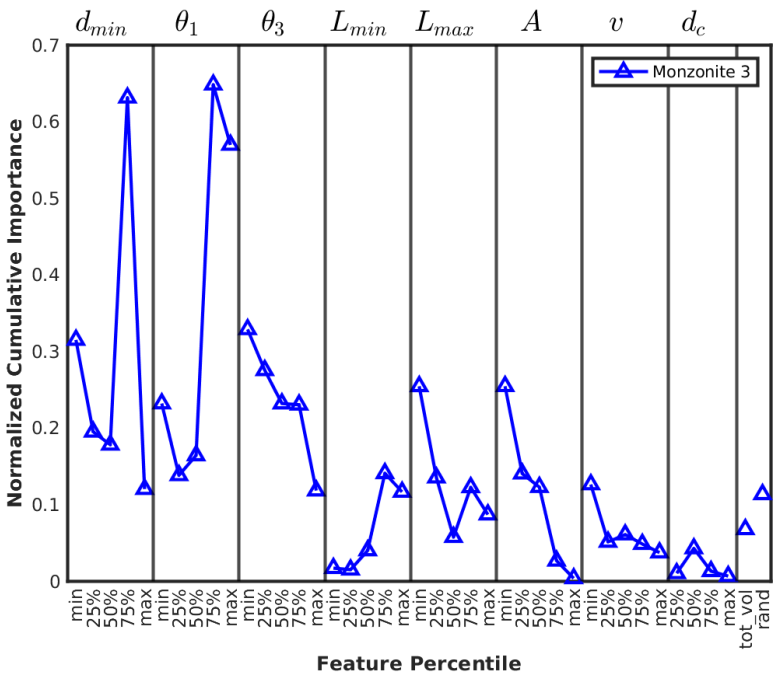

Figure A.18: Normalized cumulative importance of features for models of each monzonite experiment with R^2-scores above 0.7. The features are split by category via vertical bars, and the statistics of each feature are shown on the x-axis. The symbols and abbreviations above each column are defined in Table A.1.

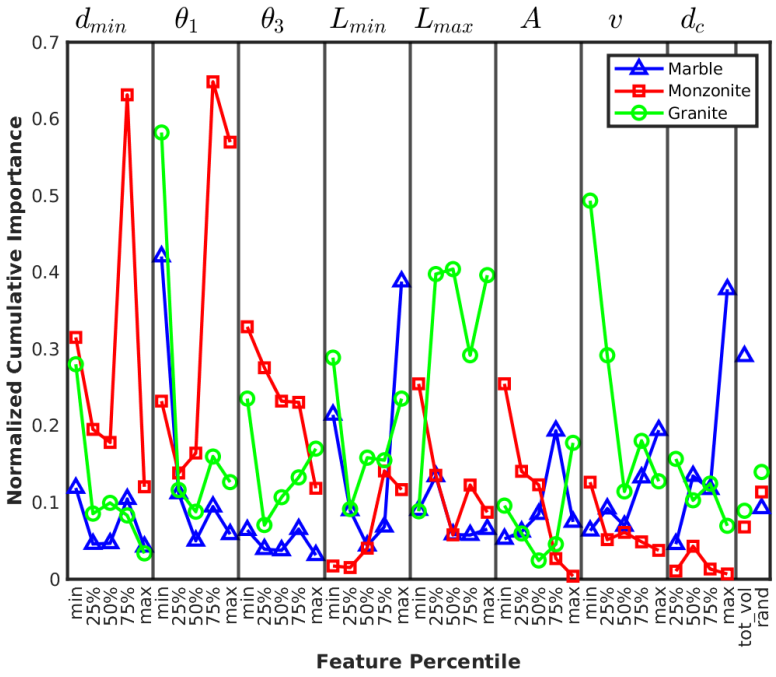

Figure A.19: Normalized cumulative importance of features for models of each each rock type with R^2-scores above 0.7. The features are split by category via vertical bars, and the statistics of each feature are shown on the x-axis. The symbols and abbreviations above each column are defined in Table A.1.

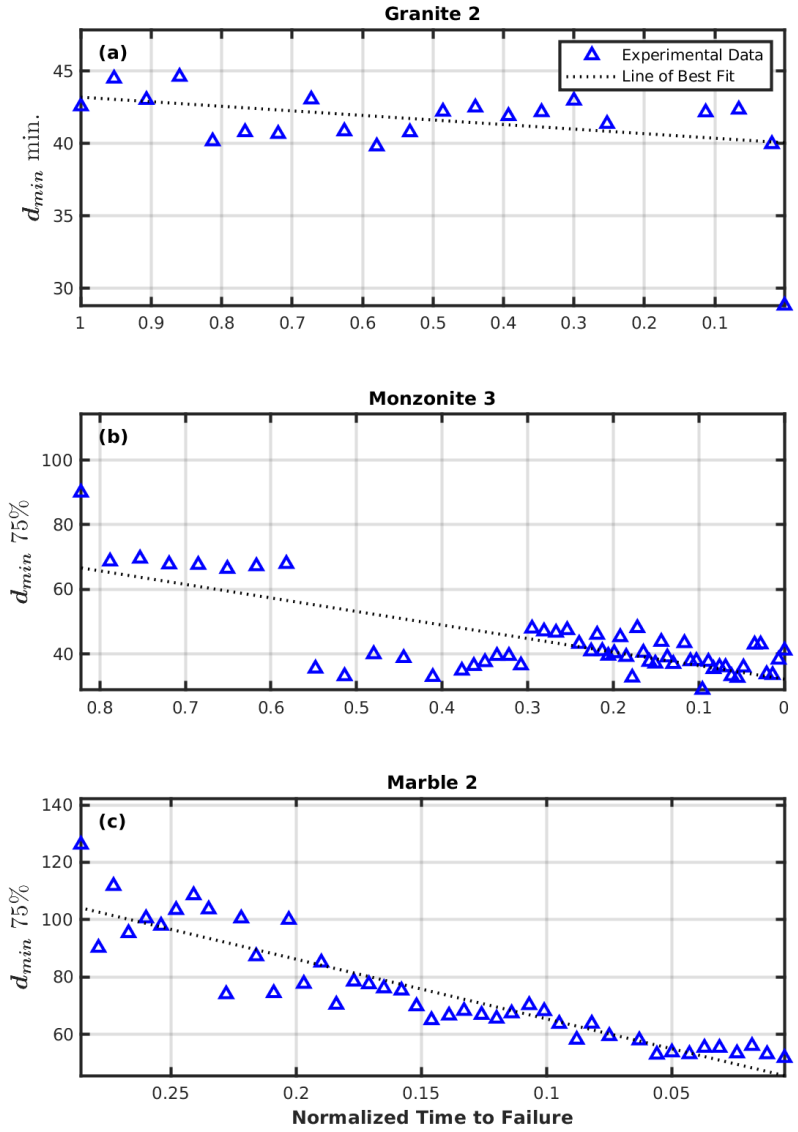

Figure A.20: The percentiles of the minimum distance between fractures $d_{\min}$ with the highest importance for experiments: Granite 2 (a), Monzonite 3 (b), and Marble 2 (c), as functions of the normalized time to failure ∇_{D}. It was in the models for these three experiments that $d_{\min}$ exhibited the highest importance.

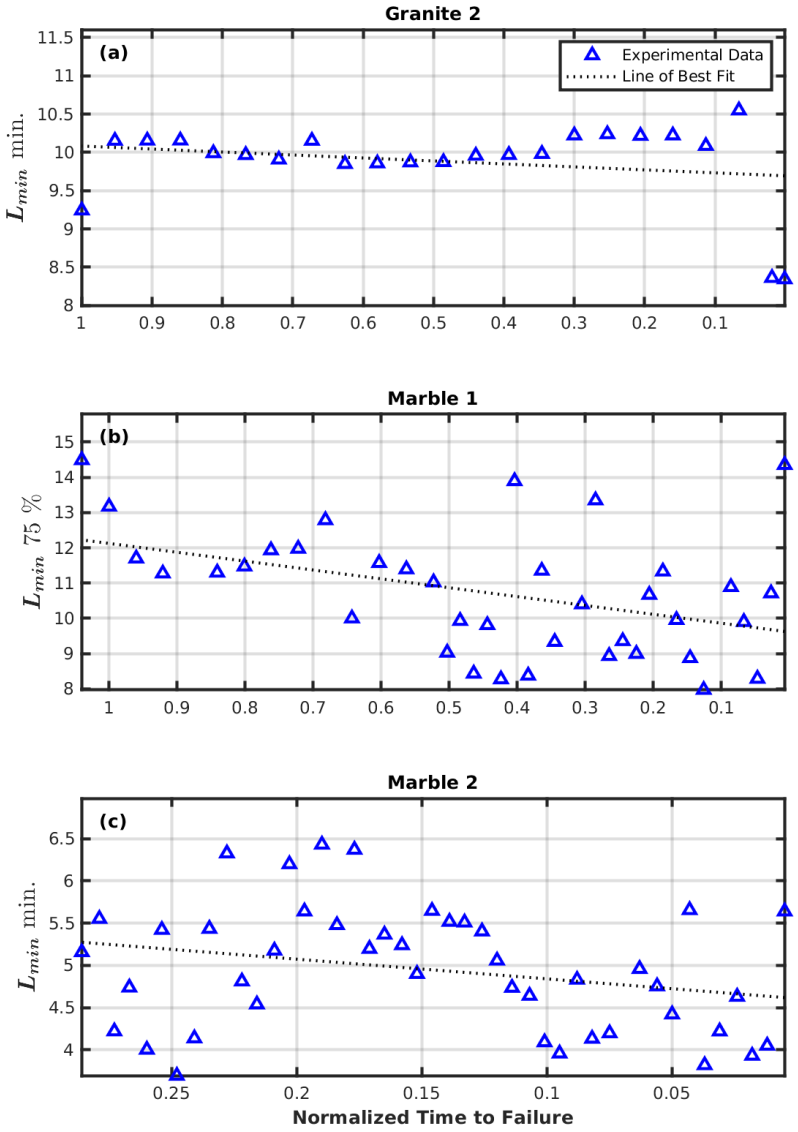

Figure A.21: The percentiles of the fracture aperture $L_{\min}$ with the highest importance for experiments: Granite 2 (a), Marble 1 (b), and Marble 2 (c), as functions of the normalized time to failure ∇_{D}. It was in the models for these three experiments that $L_{\min}$ exhibited the highest importance.

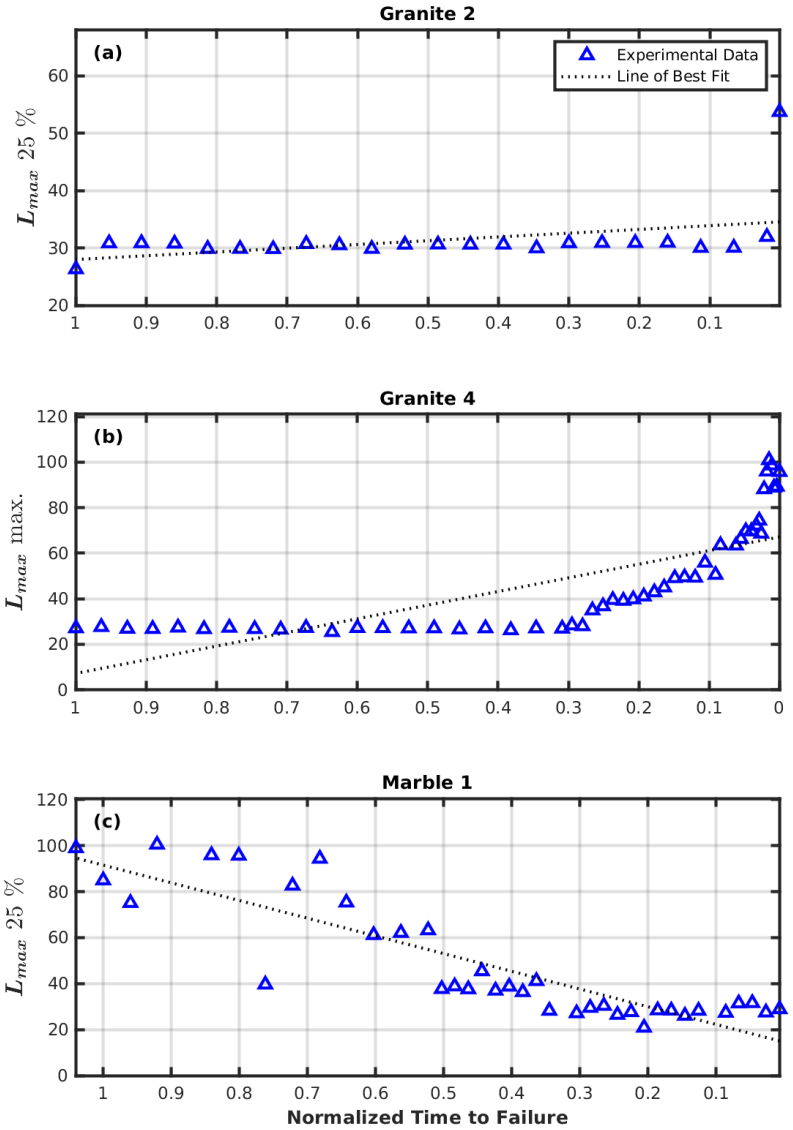

Figure A.22: The percentiles of the fracture length $L_{\max}$ with the highest importance for experiments: Granite 2 (a), Granite 4 (b), and Marble 1 (c), as functions of the normalized time to failure ∇_{D}. It was in the models for these three experiments that $L_{\max}$ exhibited the highest importance.

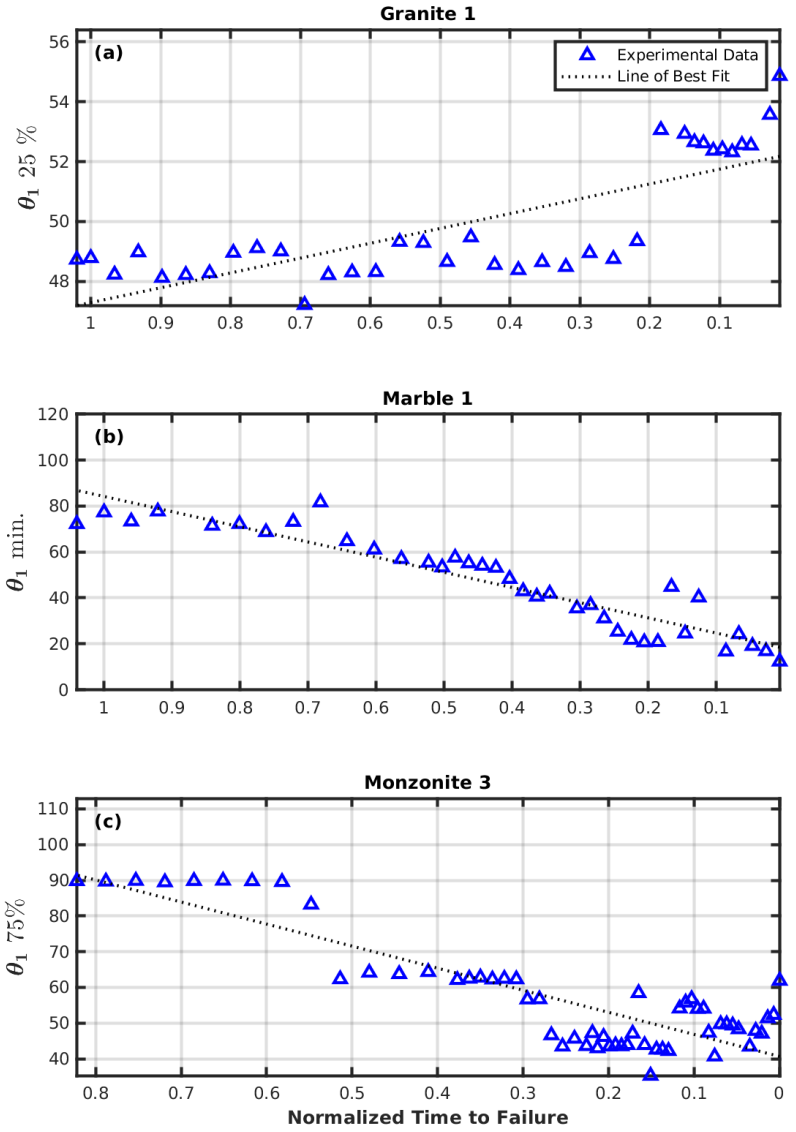

Figure A.23: The 75^{th} percentile of the orientation of the smallest fracture dimension relative to the maximum compression direction θ_1 for experiments: Granite 1 (a), Marble 2 (b), and Monzonite 3 (c), as functions of the normalized time to failure ∇_{D}. It was in the models for these three experiments that percentiles of θ_1 exhibited the highest importance.

Bibliography

Bonamy, D. and Bouchaud, E. (2011). 'Failure of heterogeneous materials: A dynamic phase transition?' In: *Physics Reports* vol. 498, no. 1, pp. 1–44.

Bordignon, N., Piccolroaz, A., Dal Corso, F. and Bigoni, D. (2015). 'Strain Localization and Shear Band Propagation in Ductile Materials'. In: *Frontiers in Materials* vol. 2.

Cartwright-Taylor, A., Main, I. G., Butler, I. B., Fusseis, F., Flynn, M. and King, A. (2020). 'Catastrophic failure: how and when? Insights from 4D in-situ x-ray micro-tomography'. In:

Chen, T. and Guestrin, C. (2016). 'XGBoost'. In: *Proceedings of the 22nd ACM SIGKDD International Conference on Knowledge Discovery and Data Mining*.

Dahlen, F. A. (1984). 'Noncohesive critical Coulomb wedges: An exact solution'. In: *Journal of Geophysical Research: Solid Earth* vol. 89, no. B12, pp. 10125–10133.

Golshani, A., Okui, Y., Oda, M. and Takemura, T. (2006). 'A micromechanical model for brittle failure of rock and its relation to crack growth observed in triaxial compression tests of granite'. In: *Mechanics of Materials* vol. 38, no. 4, pp. 287–303.

Griffith, A. A. (1921). 'VI. The phenomena of rupture and flow in solids'. In: *Philosophical Transactions of the Royal Society of London. Series A, Containing Papers of a Mathematical or Physical Character* vol. 221, no. 582-593, pp. 163–198.

Isida, M. (1971). 'Effect of width and length on stress intensity factors of internally cracked plates under various boundary conditions'. In: *International Journal of Fracture Mechanics* vol. 7, no. 3.

Jaeger, C. (2010). *Rock mechanics and engineering*. Lightning Source UK.

Kandula, N., Cordonnier, B., Boller, E., Weiss, J., Dysthe, D. K. and Renard, F. (2019). 'Dynamics of Microscale Precursors During Brittle Compressive Failure in Carrara Marble'. In: *Journal of Geophysical Research: Solid Earth* vol. 124, no. 6, pp. 6121–6139.

Lockner, D. A. (1995). In: *Rock physics amp; phase relations: a handbook of physical constants*. American Geophysical Union, pp. 127–142.

Lundberg, S. and Lee, S.-I. (2017). *A Unified Approach to Interpreting Model Predictions*. arXiv: 1705.07874 [cs.AI].

McBeck, J. A., Aiken, J. M., Mathiesen, J., Ben-Zion, Y. and Renard, F. (2020). 'Deformation Precursors to Catastrophic Failure in Rocks'. In: *Geophysical Research Letters* vol. 47, no. 24.

McBeck, J., Kandula, N., Aiken, J. M., Cordonnier, B. and Renard, F. (2019). 'Isolating the Factors That Govern Fracture Development in Rocks Throughout Dynamic In Situ X-Ray Tomography Experiments'. In: *Geophysical Research Letters* vol. 46, no. 20, pp. 11127–11135.

McBeck, J. A., Zhu, W. and Renard, F. (2021). 'The competition between fracture nucleation, propagation, and coalescence in dry and water-saturated crystalline rock'. In: *Solid Earth* vol. 12, no. 2, pp. 375–387.

Meyers, M. (2001). 'Plasticity: Adiabatic Shear Localization'. In: *Encyclopedia of Materials: Science and Technology*, pp. 7093–7103.

Olson, J. E. (2007). 'Fracture aperture, length and pattern geometry development under biaxial loading: a numerical study with applications to natural, cross-jointed systems'. In: *Geological Society, London, Special Publications* vol. 289, no. 1, pp. 123–142.

Olson, J. E. and Pollard, D. D. (1991). 'The initiation and growth of en échelon veins'. In: *Journal of Structural Geology* vol. 13, no. 5, pp. 595–608.

Paterson, M. S. (1978). *Experimental rock deformation, the brittle field.*

Renard, F., Cordonnier, B., Dysthe, D. K., Boller, E., Tafforeau, P. and Rack, A. (2016). 'A deformation rig for synchrotron microtomography studies of geomaterials under conditionsnbsp;down to 10km depth in the Earth'. In: *Journal of Synchrotron Radiation* vol. 23, no. 4, pp. 1030–1034.

Renard, F., McBeck, J. et al. (2018). 'Dynamic In Situ Three-Dimensional Imaging and Digital Volume Correlation Analysis to Quantify Strain Localization and Fracture Coalescence in Sandstone'. In: *Pure and Applied Geophysics* vol. 176, no. 3, pp. 1083–1115.

Tapponnier, P. and Brace, W. (1976). 'Development of stress-induced microcracks in Westerly Granite'. In: *International Journal of Rock Mechanics and Mining Sciences amp; Geomechanics Abstracts* vol. 13, no. 4, pp. 103–112.

Thomas, R. N., Paluszny, A. and Zimmerman, R. W. (2017). 'Quantification of Fracture Interaction Using Stress Intensity Factor Variation Maps'. In: *Journal of Geophysical Research: Solid Earth* vol. 122, no. 10, pp. 7698–7717.

Wu, X. Y., Baud, P. and Wong, T.-f. (2000). 'Micromechanics of compressive failure and spatial evolution of anisotropic damage in Darley Dale sandstone'. In: *International Journal of Rock Mechanics and Mining Sciences* vol. 37, no. 1-2, pp. 143–160.